Numerical Simulation and Experimental Study of ISAR Imaging of Spherical Convergent Flap Nozzle

Yichao Liang [1], Qingzhen Yang [2], Yongqiang Shi [2], Jin Bai [2], and Qi Lin [1*]

[1] School of Aerospace Engineering
Xiamen University, Xiamen, Fujian 361005, China
247142586@qq.com, *qilin@xmu.edu.cn

[2] School of Power and Energy
Northwestern Polytechnical University, Xi'an, Shaanxi 710072, China

Abstract ─ The research on the electromagnetic scattering characteristics of the aero-engine nozzle can provide an important reference for the electromagnetic stealth design of aircraft. In this paper, the numerical simulation and experimental measurement are used to study the radar cross section (RCS) and inverse synthetic aperture radar (ISAR) image characteristics of spherical convergence flap nozzle (SCFN). Firstly, the feasibility of using the shooting bouncing ray (SBR) method to calculate the scattering characteristics of electrically large and deep cavity is verified. Secondly, the numerical simulation data and experimental data of electromagnetic scattering of SCFN are processed by ISAR imaging algorithm, the numerical and experimental ISAR images of SCFN are obtained. The results show that SBR can effectively calculate the RCS of the electrically large size cavity within ± 30° of the axis direction. The polarization influences the experimental ISAR image. Both the numerical and the experimental ISAR image can accurately reflect the scattering center distribution inside the SCFN, and the numerical ISAR image is superior to the experimental ISAR image in image entropy and equivalent number of looks (ENL), and is partly inferior to the experimental ISAR image in terms of image average gradient. The results prove the validity and accuracy of the numerical ISAR image.

Index Terms ─ Inverse Synthetic Aperture Radar (ISAR), shooting and bouncing ray (SBR), scattering center, spherical convergence flap nozzle (SCFN).

I. INTRODUCTION

For the military aircraft, the aero-engine nozzle produces a significant impact on the backscattering of aircraft. Therefore, whether the electromagnetic scattering of the engine nozzle can be effectively controlled is directly related to the backward electromagnetic stealing capability of the aircraft. As a representative of a new type of vector nozzle, spherical convergent flap nozzle (SCFN) has superior aerodynamic and stealth performance. Due to its simple structure, large vectoring angle and easy integration with the aircraft, SCFN has been included in the integrated high performance turbine engine technology (IHPTET) program by the United States [1].

Inverse synthetic aperture radar (ISAR) has been widely used in the military field, it has mainly been applied to automatic recognition and stealth of targets in recent years. Because of the particularity of the field, there is less information on the ISAR imaging of real military aircraft. Besides, there are few published results in the ISAR imaging of aircraft with the inlet and nozzle, and it is rare to directly study the ISAR imaging of aero-engine nozzle. ISAR imaging of the engine nozzle can analyze the strong scattering source inside the nozzle and guide its radar cross section (RCS) reduction, which would help improve the backward electromagnetic stealth performance of the aircraft and also provide a reference to the aerodynamic design of the engine nozzle.

In 1990, Lin et al. conducted the first electromagnetic scattering test on the S-shape inlet and obtained the RCS and ISAR images of the S-shape inlet [2]. However, due to the underdeveloped computer graphics technology, the ISAR image was very blurred and could not reflect the distribution of the scattering center clearly. In recent years, Guo et al. tested the electromagnetic scattering characteristics of the axisymmetric nozzle and the double S-shape nozzle respectively, and obtained a relatively clear ISAR image [3, 4]. Although measurement in anechoic chamber is an effective and accurate method, the current testing device is difficult to measure full pitch/yaw angles for large targets. The numerical simulation of ISAR imaging of the target can make up for this shortcoming.

To obtain numerical ISAR image, it is necessary to calculate the scattering data of the target over a range

Submitted On: April 16, 2019
Accepted On: April 12, 2020

of frequencies and angles. For electrically large size cavities, the full wave methods such as method of moment (MOM) or finite element method (FEM) consume too much computational resources [5], so high frequency approximation methods such as shooting and bouncing rays (SBR) are the main methods currently used. In recent years, in order to accelerate the calculation speed and accuracy of ISAR images, the traditional SBR has many improved methods, such as the Ray Travel Map (RTM) method in [6]; image-domain ray tube integral equation method proposed in [7, 8]; Jiang et al. used OpenGL to speed up ray tracing in the SBR [9]; Dong et al. added the EEC method to the SBR to correct the contribution of edge diffraction [10]. However, the models studied by the above scholars are closed targets, and the ISAR images lack experimental verification. Sze studied the ISAR image of electrically large zigzag-grooved structures [11], but the model differs greatly from the actual inlet or nozzle; Pienaar et al. performed numerical simulation and experimental tests on the electromagnetic scattering characteristics of the Boe707 model [12, 13]. However, the inlet of the model was closed and could not reflect the scattering characteristics of the cavity. In summary, it is necessary to conduct numerical simulation and experimental verification of ISAR imaging of electrically large cavity.

In this paper, the numerical calculation and experimental test of electromagnetic scattering characteristics of SCFN under different frequencies and different polarization modes are conducted. Firstly, the RCS of SCFN obtained by SBR and measurement are compared, and the effectiveness of SBR in calculating the electromagnetic scattering characteristics of the electrically large and deep cavity with complex internal structure is verified. Secondly, the numerical ISAR image and experimental ISAR image of SCFN are acquired by imaging algorithm and compared through different criteria. Finally, the effects of frequency, polarization mode and experimental procedure on ISAR images are analyzed.

II. SBR METHOD AND VERIFICATION

For an arbitrary tube, the scattered electric field at observation point A (r,θ,φ) is [14]:

$$\boldsymbol{E}(r,\theta,\varphi)=\frac{e^{-jkr}}{r}(\hat{\theta}A_{\theta}+\hat{\varphi}A_{\varphi}). \tag{1}$$

According to the Huygens' principle, A_θ and A_φ can be obtained by the following formula:

$$\begin{bmatrix}A_{\theta}\\A_{\varphi}\end{bmatrix}=\sum_{i=1}^{N}\begin{bmatrix}B_{\theta}\\B_{\varphi}\end{bmatrix}\left(\frac{jk}{2\pi}\right)(\Delta A)_{exit}S(\theta,\varphi)e^{j\hat{k}r_A}, \tag{2}$$

with

$$\begin{aligned}B_{\theta}&=-s_1E_3\cos\varphi-s_2E_3\sin\varphi+s_3(E_1\cos\varphi+E_2\sin\varphi),\\B_{\varphi}&=s_1(E_3\cos\varphi\sin\varphi+\sin\theta E_2)+s_2(-E_1\sin\theta-\\&E_3\cos\theta\cos\varphi)+s_3(E_2\cos\theta\cos\varphi-E_1\cos\theta\sin\varphi).\end{aligned} \tag{3}$$

Where N is the total number of the effective ray tubes, r_A is the position vector of the last hit point on the target, $s(\theta,\varphi)$ is the shape function, ΔA_{exit} is the cross section of the exit ray tube. $\boldsymbol{E}(A)=E_1\hat{x}+E_2\hat{y}+E_3\hat{z}$, $\boldsymbol{E}(A)$ is the electric field with each ray tube, $\boldsymbol{s}=s_1\hat{x}+s_2\hat{y}+s_3\hat{z}$, $\boldsymbol{s}$ is the exit ray tube direction, and $\boldsymbol{k}=k_1\hat{x}+k_2\hat{y}+k_3\hat{z}$, $\boldsymbol{k}$ is the observation wave vector.

To improve the calculation accuracy, 1/20 wavelength is chosen as the step size for dividing the ray tube. For accelerating the computational efficiency of the intersection of the ray and the triangle, a data structure based on the Bounding Volume Hierarchy BVH) method is employed.

In order to verify the accuracy of the SBR, the RCS of SCFN calculated by SBR and measurement are compared. The structure of the SCFN is shown in Fig. 1. The incident angle of the plane wave is θ = 90°, φ = -30° to 30°. The SCFN has a central cone and mixer inside, and the inlet of SCFN is disposed as metal terminal. The comparison between the calculated results and the experimental results are shown in Fig. 2.

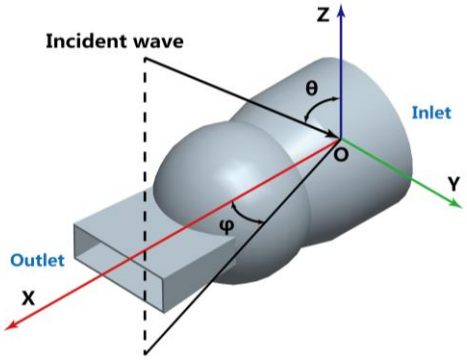

(a) SCFN and Coordinate System

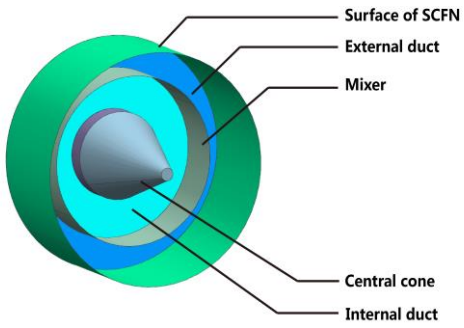

(b) The bottom of SCFN

Fig. 1. SCFN geometric model and local profile.

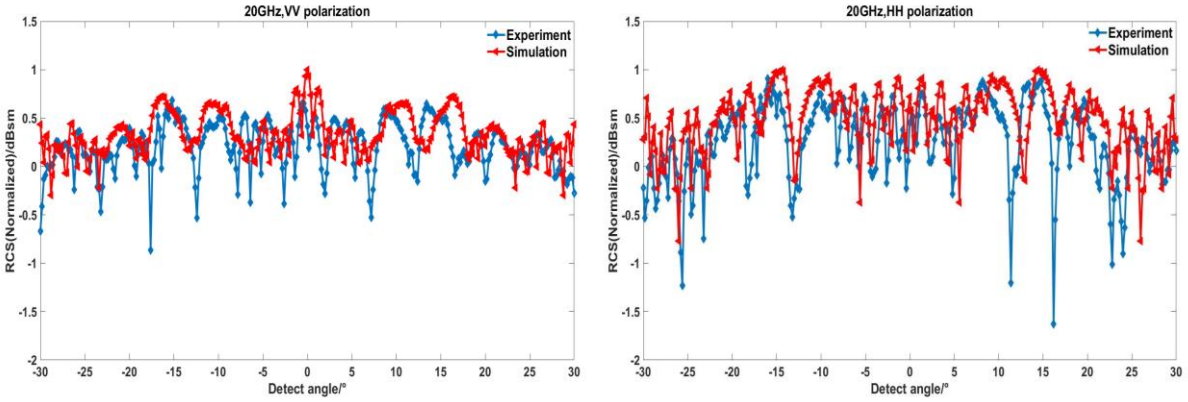

(a) Vertical polarization (b) Horizontal polarization

Fig. 2. Comparison of SCFN's RCS: "Experiment" (blue dots and line), and "simulation" (red dots and line).

Figure 2 illustrates normalized RCS of SCFN obtained by SBR and measurement at 20 GHz and different polarization modes. It can be seen from Fig. 2 that the RCS of experimental result at 0° is not the peak value because the adjustment of the nozzle central axis is difficult to implement during the test, which causes some deviation in detection angle. From the comparison results of RCS curves in Fig. 2, the simulation results are close to the experimental results. The simulation results of horizontal polarization agree well with the experimental results in the range of ±30° while there are certain errors at vertical polarization. The difference between the numerical results and the experimental results is partly due to the inevitable error in model manufacturing. The anechoic chamber background also has a cluttered effect on the test results, which can be reduced by background vector canceling, but the influence cannot be completely eliminated. In general, the SBR has certain accuracy and reliability when calculating electromagnetic scattering characteristics of electrically large and deep cavity.

III. ISAR IMAGING ALGORITHM

In this paper, the filtered back projection method (FBP) is used to reconstruct the ISAR image. The relationship between the scattering field and the image is given by the following formula [15, 16]:

$$g(x,y)=\int_{\theta_{\min}}^{\theta_{\max}}\int_{k_{\min}}^{k_{\max}} kG(k,\theta)\exp[j2\pi k(y\cos\theta - x\sin\theta)]dkd\theta. \quad (4)$$

Where $g(x,y)$ is the ISAR image of the target, $G(k,\theta)$ is the scattering filed of measured or calculated. $k=2\pi/\lambda$, λ is wavelength, θ is the azimuth angle, as Fig. 3 shows. Then (4) can be decomposed into:

$$p_\theta(l)=\int_0^B (k+k_{\min})G(k+k_{\min},\theta)\exp(j2\pi kl)dk, \quad (5)$$

$$g(x,y)=\int_{\theta_{\min}}^{\theta_{\max}} p_\theta(l)\exp(j2\pi k_{\min}l)d\theta, \quad (6)$$

$$l=y\cos\theta - x\sin\theta. \quad (7)$$

Where $B=k_{\max}-k_{\min}$. Since the frequencies in the calculation and measurement are discrete, it is necessary to discretize (5) and (6). If $k=nB/N$, n=0, 1…, N-1, N is number of sampling frequency points, then (5) can be rewritten as:

$$p_\theta(l)=\sum_{n=0}^{(N-1)B/N}(\frac{B}{N}n+k_{\min})G(n,\theta)\exp(j2\pi\frac{B}{N}nl). \quad (8)$$

The projection line l is equidistantly discretized according l_m, $l_m=m/B$, m=0,1,…,N-1:

$$\text{let } G_\theta(n)=(\frac{B}{N}n+k_{\min})G(n,\theta), \text{ then,}$$

$$p_\theta(l_m)=\sum_{n=0}^{N-1}G_\theta(n)\exp(j2\pi\frac{m}{N}n)=IFFT[G_\theta(n)]. \quad (9)$$

Where $p_\theta(l_m)$ is the projection value obtained from different l_m. The projection line l in the process of integration changes with θ. For $g(x,y)$ at any point, each θ corresponds to a different l. Therefore, $p_\theta(l)$ is the projection value obtained from the discrete l, and $p_\theta(l_m)$ needs to be obtained by interpolating $p_\theta(l_m)$:

$$p_\theta(l)=\text{interp}[p_\theta(l_{m-1}),p_\theta(l_m)]. \quad (10)$$

"Interp" means the interpolation method. In this paper, linear interpolation is selected as interpolation method. Finally, the ISAR image can be obtained by integrating angle:

$$g(x,y)=\int_{\theta_{\min}}^{\theta_{\max}} p_\theta(l)e^{j2\pi k_{\min}l}d\theta=\sum_\theta p_\theta(l)e^{j2\pi k_{\min}l}. \quad (11)$$

It can be seen from the above analysis that the formula derivation process of the FBP method is strict, and only the interpolation process brings errors. In

addition, in order to reduce the side lobes, Kaiser window function is used.

IV. ISAR IMAGING STUDY OF SCFN

A. Numerical simulation of ISAR imaging of SCFN

In this paper, SBR is used to calculate the electromagnetic scattering characteristics of SCFN. The frequency is the same as the experiment, which is 3 to 6 GHz, 8 to 12 GHz, 19 to 25 GHz respectively; the polarization modes are horizontal polarization and vertical polarization; the incident angle is θ = 90°, φ = -20°~20°. The calculation results are given together with the experimental results for comparison.

B. Experimental test of ISAR imaging of SCFN

The measurement was conducted in the National Defense Key Laboratory of UAV Special Technology of Northwestern Polytechnical University. The experiment used a stepped-frequency test system. The stepped-frequency signal is generated by Agilent E8363A VNA. The experiment uses broadband horn antenna HD-1060, its bandwidth is 1-6GHz, the gain is 6-13dB; standard gain horn antenna HD-100 and HD220, bandwidth is 8.20-12.40GHz and 17.6-26.7GHz respectively, and the gain is 15dB. The cross polarization gain of the antenna is less than 30 dB of the main polarization gain.

To test the electromagnetic scattering characteristics inside the SCFN, the low electromagnetic scattering characteristic carrier (hereinafter referred to as a carrier) was designed and fabricated. The outside of the carrier is covered with radar absorbing material. The SCFN is wrapped in a carrier as shown in Fig. 4.

The measurement system construction is shown in Fig. 5. The vector network analyzer transmits the stepped-frequency signal, which is amplified by a power amplifier and then transmitted, finally received by the horn antenna. To minimize the influence of the coupling signals on measurement accuracy, some radar absorbing materials were placed between the two antennas during the measurement.

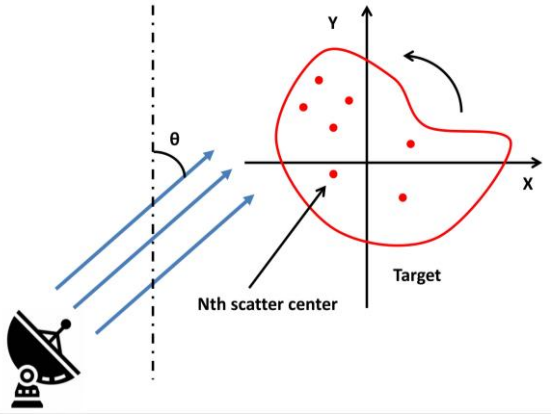

Fig. 3. Schematic diagram of turntable imaging.

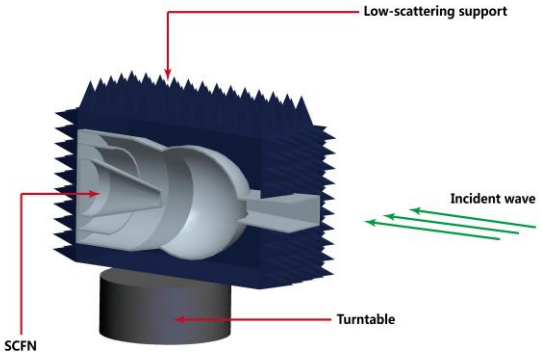

(a) The profile of SCFN and carrier

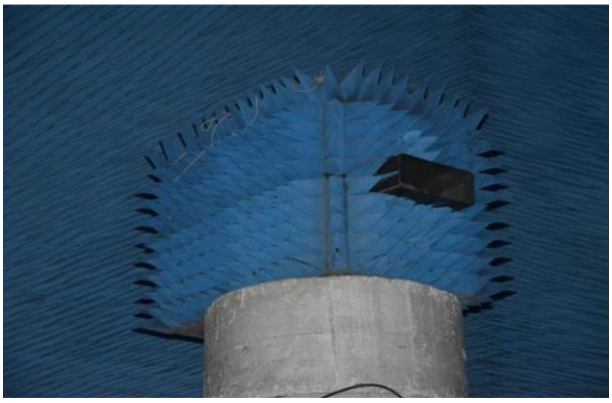

(b) The testing SCFN model

Fig. 4. The structure of testing SCFN.

C. Comparison between numerical simulation and experimental results

The results of numerical simulation and experimental testing of the ISAR imaging of the SCFN are shown in Fig. 6 to Fig. 8. The ISAR image of the cavity structure does not reflect the geometry of the cavity and only gives the distribution of the scattering center inside the cavity. For ease of understanding, the outline of the SCFN is supplemented, as depicted by the red lines in Fig. 6 to Fig. 8. For the sake of simplicity and not to cause misunderstanding, the ISAR image based on numerical simulation is simply referred to as "numerical ISAR image", and the ISAR image based on experimental test is simply referred to as "experimental ISAR image.

Figure 6 shows ISAR imaging results at 3 to 6 GHz. Both the calculation results and the experimental results show that when electromagnetic wave entered inside the SCFN, the bottom of SCFN contributes the most to scattering because the scattering type at the bottom is specular scattering. Since electromagnetic

wave bounces multiple times between the mixer and the center cone, the scattering in this area is also strong. It can be seen from the experimental results in Fig. 6 (b) and Fig. 6 (d) that the carrier also has a certain scattering intensity.

It can be seen from the experimental ISAR images under different polarization modes that the outlet of SCFN shows two spots under vertical polarization and a stripe under horizontal polarization. The experimental results show that polarization has different effects on scattering, mainly because the edge diffraction intensity caused by polarization is different. When the edge is parallel to the direction of polarization, the edge will produce strong edge diffraction; conversely, when the edge is perpendicular to the direction of polarization, the resulting edge diffraction intensity is much weaker. In addition, since the surface of the SCFN is not smooth, electromagnetic waves are diffusely reflected, and the outlet is not completely wrapped by the carrier during measurement, so the outlet can be clearly seen in the experimental results. The outlet cannot be represented in numerical results because all surfaces in the calculation were treated as non-thickness surfaces, and SBR ignores the edge diffraction in the calculation and considers all regions as ideal conductors, diffuse reflection does not exist.

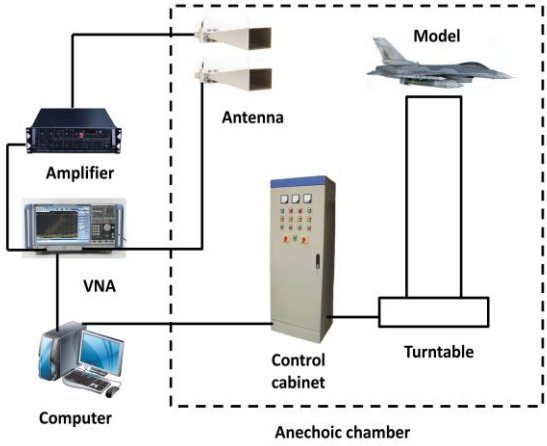

Fig. 5. Diagram of measurement system.

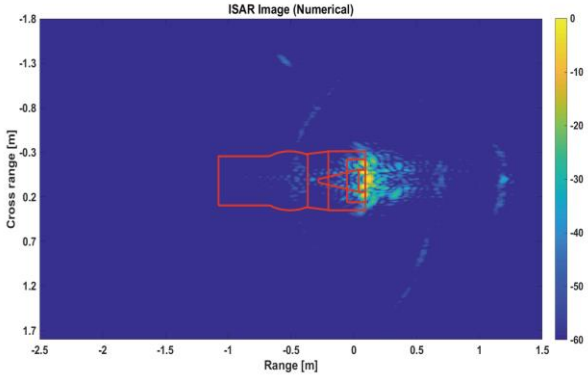

(a) Numerical ISAR Image (vertical polarization)

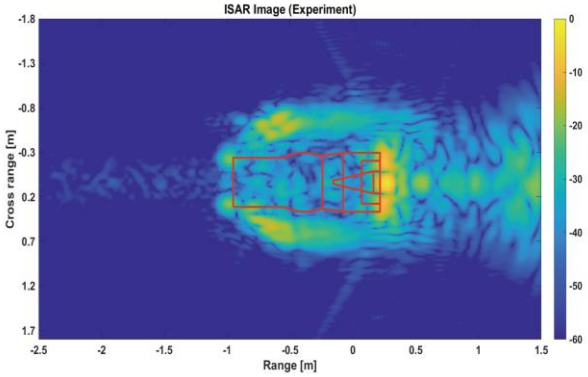

(b) Experimental ISAR Image (vertical polarization)

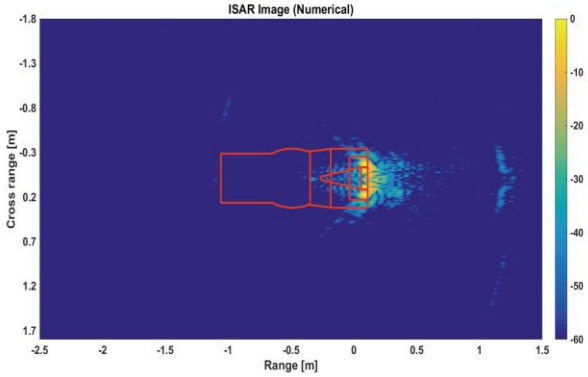

(c) Numerical ISAR Image (horizontal polarization)

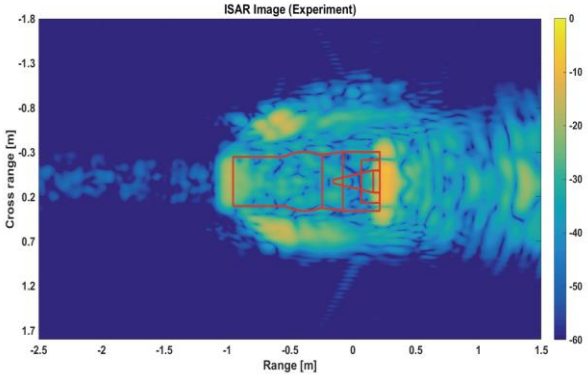

(d) Experimental ISAR Image (horizontal polarization)

Fig. 6. Comparison between numerical and experimental ISAR image (3 to 6GHz).

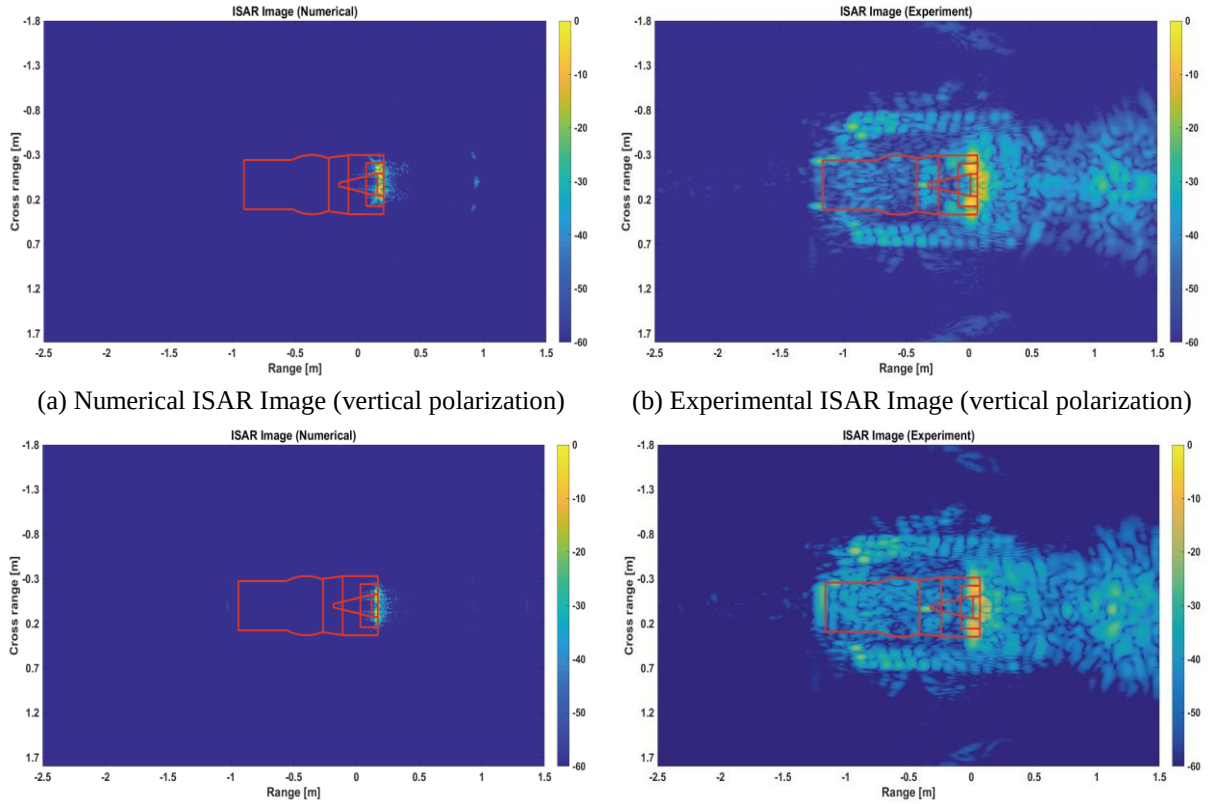

(a) Numerical ISAR Image (vertical polarization)

(b) Experimental ISAR Image (vertical polarization)

(c) Numerical ISAR Image (horizontal polarization)

(d) Experimental ISAR Image (horizontal polarization)

Fig. 7. Comparison between Numerical and Experimental ISAR Image (8 to 12GHz).

Figure 7 shows ISAR imaging results at 8 to 12 GHz. The center cone of SCFN is a truncated cone which has a small flat surface at the top. The type of scattering of this small flat surface is the same as the bottom of SCFN, both of which are specular scattering. However, since the area of the top of center cone is too small, the scattering intensity is much smaller than the bottom of SCFN. In Fig. 7, it is faintly visible that there is a bright spot at the position corresponding to the top of the center cone.

Figure 8 shows the imaging results at 19 to 25 GHz. The scattering intensity of the carrier in Fig. 8 is much smaller than that of Fig. 6 and Fig. 7, because the radar absorbing material has a better absorption effect in the high frequency band and a poor effect in the low frequency band. The bright spots produced by the top of the center cone are clearly visible in Fig. 8. As bandwidth and frequency increase, the resolution of the ISAR increases accordingly, so that the absorbing pyramid on the carrier can be clearly distinguished in Fig. 8. In numerical ISAR images and experimental ISAR images, the region outside SCFN also has scattering intensity, which is mainly due to interference caused by imaging algorithm. In addition, the manufacturing error of SCFN, antenna measurement error, darkroom background interference, etc. will cause disturbance to the experimental ISAR image.

In order to quantitatively evaluate the quality of ISAR images, Shannon entropy, equivalent number of looks (ENL) and image average gradient are taken as the criteria for evaluating the quality of ISAR images [17]. For an ISAR image in size of $M \times N$, define the Shannon entropy *H(f)* as:

$$H(f) = -\sum_{m=1}^{M}\sum_{n=1}^{N} P_{mn} \ln P_{mn}, \tag{12}$$

where

$$P_{mn} = \frac{f(m,n)}{\sum_{m=1}^{M}\sum_{n=1}^{N} f(m,n)}. \tag{13}$$

$f(m,n)$ represents the gray value of the pixel at (m,n) in the ISAR image. The smaller entropy value of ISAR image is, the more information of ISAR image contains, the better the focusing performance of ISAR image has.

ENL is an index to measure the relative intensity of speckle noise in an image. The larger the ENL is, the better the identifiability is, and the weaker the speckle is. It is defined as:

$$ENL = \frac{E(I)^2}{\mathrm{var}(I)}. \quad (14)$$

Where $E(I)$ and $\mathrm{var}(I)$ represent the mean and variance of the image respectively.

The average gradient of the image indicates the rate at which the image details change and represents the relative clarity of the image. The larger the average gradient is, the clearer the image is. It is defined as:

$$G = \frac{1}{M \times N} \sum_{i=1}^{M} \sum_{j=1}^{N} \sqrt{((\frac{\partial f}{\partial x})^2 + (\frac{\partial f}{\partial y})^2) / 2}. \quad (15)$$

Where $M \times N$ denotes the image size, $\frac{\partial f}{\partial x}$ denotes the horizontal gradient, and $\frac{\partial f}{\partial y}$ denotes the vertical gradient.

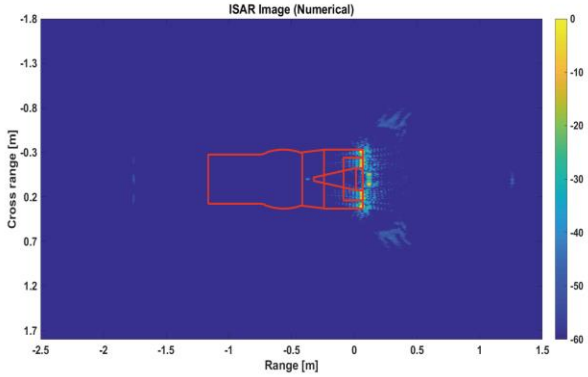

(a) Numerical ISAR Image (vertical polarization)

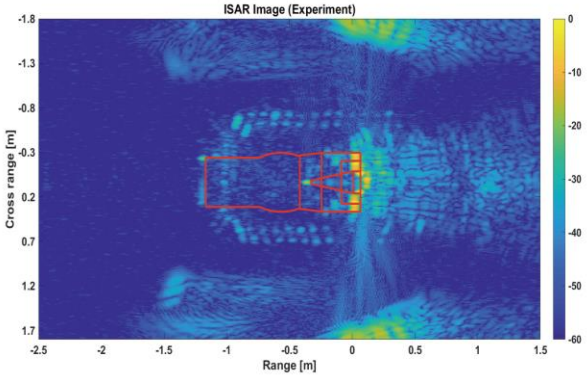

(b) Experimental ISAR Image (vertical polarization)

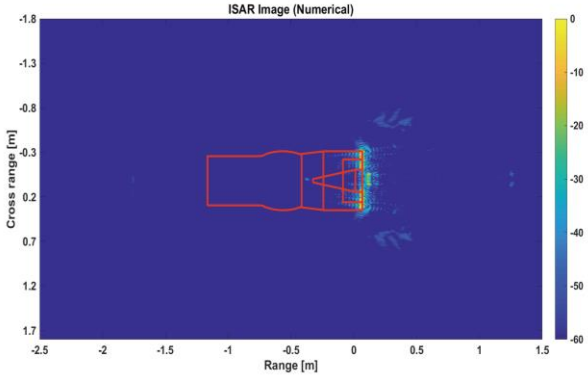

(c) Numerical ISAR Image (horizontal polarization)

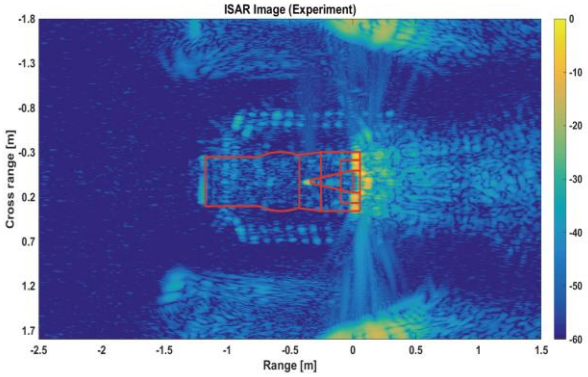

(d) Experimental ISAR Image (horizontal polarization)

Fig. 8. Comparison between numerical and experimental ISAR image (19~25 GHz).

It can be seen from Table 1 and Table 2 that different polarization modes have little effect on the entropy of ISAR image, and numerical ISAR image entropy is smaller than the entropy of experimental ISAR image, which indicates that the focusing performance of numerical image is better than that of experimental image. The ENL of the numerical ISAR image is larger than that of the experimental ISAR image, indicating that the experimental ISAR image is difficult to identify, which may due to the strong interference in the experimental process. The image average gradient characterizes the intensity of the image change. Since the numerical ISAR image has no background and carrier interference, most areas of the image do not change much, so the image average gradient of the numerical ISAR image is smaller.

Comparing the imaging results we can infer that the area where SCFN contributes mainly to scattering is the part where specular reflection exists, the part where multiple bouncing occurs, and the part where edge diffraction occurs. Since the SBR considers the environment around the target to be vacuum when calculating the target electromagnetic scattering, there is no anechoic chamber background interference, thus the numerical ISAR image is visually clearer than experimental ISAR image. Compared to experimental ISAR images with various disturbances, numerical ISAR images can be better applied to the target recognition. In addition, since the numerical ISAR image can accurately reflect the scattering center distribution inside the SCFN, the numerical ISAR image can be applied to the RCS extraction to judge

the contribution of the internal components of SCFN to total scattering. Taking into account the enormous resources spent on ISAR imaging experiment, the advantages of numerical ISAR images in terms of cost and efficiency are more obvious.

Table 1: Results of each criterion under horizontal polarization

Frequency (GHz)	**3-6**		**8-12**		**19-25**	
Criterion	Num.	Exp.	Num.	Exp.	Num.	Exp.
Image entropy	0.4361	2.9995	0.1123	2.5781	0.2469	3.7061
ENL	21.1856	5.2411	82.7427	7.2330	71.8607	8.1126
Average gradient	0.0076	0.0023	0.0056	0.0097	0.0023	0.0096

*Num.: Numerical; Exp.: Experimental

Table 2: Results of each criterion under vertical polarization

Frequency (GHz)	**3-6**		**8-12**		**19-25**	
Criterion	Num.	Exp.	Num.	Exp.	Num.	Exp.
Image entropy	0.5013	3.0446	0.1968	2.6167	0.3072	3.7858
ENL	20.6227	5.6650	31.7412	7.2334	27.8587	9.1920
Average gradient	0.0107	0.0120	0.0105	0.0122	0.0109	0.0108

*Num.: Numerical; Exp.: Experimental

CONCLUSION

In this paper, the RCS characteristics and ISAR image of SCFN are numerically calculated and experimentally tested. The conclusions are as follows.

(1) The comparison with the existing experimental data shows that the SBR can accurately calculate the scattering characteristics of the electrically large and deep cavity in the axial range of ± 30°.

(2) The experimental results indicate that there are differences in the effects of polarization modes on the scattering characteristics of binary vector nozzles. The main reason for the differences is the relative positional relationship between the surface of the outlet and the polarization direction.

(3) The numerical ISAR image is superior to the experimental ISAR image in image entropy and ENL, and the average gradient of the experimental ISAR image is partly better than the experimental ISAR image. The comparison between the experimental ISAR image and the numerical ISAR image demonstrates that the ISAR image can accurately reflect the scattering center distribution inside the SCFN, so the RCS of the target component can be extracted from the ISAR image, which is also the direction of future work.

AKNOWLEDGEMENT

The author would like to sincerely appreciate the Key Laboratory of UAV Special Technology of Northwestern Polytechnical University for providing technical support for experimental testing, as well as the vigorous support of A. P Chen Weijun and A. P Hu Chufeng during experimental testing and the valuable guidance given in the writing.

REFERENCES

[1] X. Guo, Q. Z. Yang, Y. Q. Shi, and H. Q. Yang, "Effects of vector angle on RCS of spherical convergent flap nozzle," *Journal of Propulsion Technology*, vol. 39, no. 4, pp. 785-791, Apr. 2018.

[2] L. Lin and W. Chen, "Experimental study on radar scattering characteristics of S-shaped inlet," *Aerodynamic Missile Journal*, no. 05, pp. 41-46, May 1990.

[3] X. Guo, Q. Z. Yang, Y. Q. Shi, and H. C. Yang, "RCS measurement of axisymmetric nozzle under different radar overlook angle," *Journal of Propulsion Technology*, vol. 38, no. 8, pp. 1747-1753, Aug. 2017.

[4] X. Guo, Q. Yang, H. Yang, and K. Du, "Radar cross section measurement of double S-shaped nozzle with radar absorbing material," in *Selected Papers of the Chinese Society for Optical Engineering Conferences held October and November 2016*, Ed., pp. 102553H, International Society for Optics and Photonics, 2017.

[5] K. Zhang, C. Wang, and J. Jin, "Broadband monostatic RCS and ISAR computation of large and deep open cavities," *IEEE Transactions on Antennas and Propagation*, vol. 66, no. 8, pp. 4180-4193, Aug. 2018.

[6] Y. H. Lee, J. H. Bae, B. S. Kang, S. J. Lee, and K. T. Kim, "Acceleration of monostatic shooting and bouncing ray method for inverse synthetic aperture radar image generation," *Microwave and Optical Technology Letters*, vol. 58, no. 8, pp. 1848-1855, Aug. 2016.

[7] X. Y. He, X. Y. Zhou, and T. J. Cui, "Fast 3D-ISAR image simulation of targets at arbitrary aspect angles through nonuniform fast fourier transform (NUFFT)," *IEEE Transactions on Antennas and Propagation*, vol. 60, no. 5, pp. 2597-2602, May 2012.

[8] J. Lee, D. Yun, H. Kim, W. Yang, and N. Myung, "Fast ISAR image formations over multiaspect angles using the shooting and bouncing rays," *IEEE Antennas and Wireless Propagation Letters*, vol. 17, no. 6, pp. 1020-1023, June 2018.

[9] W. Jiang, M. Zhang, D. Nie, and Y. Jiao, "Improved GO/PO method and its application to wideband SAR image of conducting objects over rough surface," *Waves in Random and Complex Media*, vol. 28, no. 2, pp. 310-325, Feb. 2018.

[10] C. Dong, H. Ren, H. Yin, and C. Wang, "Efficient

full-polarized ISAR image simulation of complex target with rough surfaces," *Acta Aeronautica et Astronautica Sinica*, vol. 37, no. 4, pp. 1272-1280, Apr. 2016.

[11] K. Y. Sze and S. Kashyap, "Scattering center modeling of electrically large zigzag-grooved structures," Ed., pp. 6401-6405, IEEE, 2012.

[12] C. Pienaar, J. W. Odendaal, J. C. Smit, J. E. Cilliers, and J. Joubert, "RCS results for an electrically large realistic model airframe," *Applied Computational Electromagnetics Society Journal*, vol. 33, no. 1, pp. 87-90, Jan. 2018.

[13] J. Joubert, C. Pienaar, J. C. Smit, J. W. Odendaal, and J. E. Cilliers, "RCS validation of asymptotic techniques using measured data of an electrically large complex model airframe," *Applied Computational Electromagnetics Society Journal*, vol. 32, no. 1, pp. 60-67, Jan. 2017.

[14] H. Ling, R. C. Chou, and S. W. Lee, "Shooting and bouncing rays: calculating the RCS of an arbitrarily shaped cavity," *Antennas & Propagation IEEE Transactions on*, vol. 37, no. 2, pp. 194-205, Feb. 1989.

[15] C. Hu, N. Li, W. Chen, and L. Zhang, "High-precision RCS measurement of aircraft's weak scattering source," *Chinese Journal of Aeronautics*, vol. 29, no. 3, pp. 772-778, May 2016.

[16] N. Li, Z. Xu, C. Hu, J. Dang, and S. Guo, "Research on accurate radar cross section measurement method based on imaging extraction," *Chinese Journal of Scientific Instrument*, vol. 38, no. 1, pp. 74-82, Jan. 2017.

[17] J. Y. Wei and Z. Yan, "Research on ISAR image quality evaluation," *Systems Engineering and Electronics*, vol. 37, no. 2, pp. 298-303, Feb. 2015.